CHEMISTRY OF MATERIALS

ARTICLE

pubs.acs.org/cm

Real Structure and Thermoelectric Properties of GeTe-Rich Germanium Antimony Tellurides

Tobias Rosenthal,[†] Matthias N. Schneider,[†] Christian Stiewe,[‡] Markus Döblinger,[†] and Oliver Oeckler*,[†]

[†]Department of Chemistry, Ludwig Maximilian University Munich, Butenandtstrasse 5-13 (D), D-81377 Munich, Germany

[‡]German Aerospace Center, Linder Höhe, 51147 Cologne, Germany

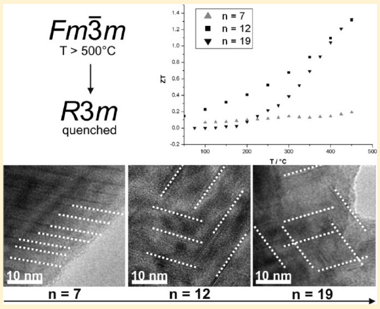

ABSTRACT: Quenched Ge−Sb−Te (GST) compounds exhibit strongly disordered metastable structures whose average structure corresponds to a distorted rocksalt type with trigonal symmetry. Depending on the composition and thermal treatment, the metrics remain more or less pseudocubic. The corresponding stable phases show regular sequences of distorted rocksalt-type blocks that formally result from layer-like cation defect ordering. These thermodynamically stable layered phases can gradually be approached by annealing the metastable (pseudo)cubic compounds that are accessible by quenching high-temperature phases. The relaxation of Te atoms in the vicinity of the defect layers leads to van der Waals gaps rather than defect layers in an undistorted matrix. The partially ordered phases obtained show defect layers with an average distance and arrangement depending on the composition and the thermal treatment of the samples. This variation of the nanostructure influences the lattice thermal conductivity (κ_L) and thus the thermoelectric figure of merit (ZT). This results in ZT values up to 1.3 at 450 °C for bulk samples of $Sb_2Te_3(GeTe)_n$ (n = 12 and 19). The stability ranges of the various phases have been examined by temperature programmed X-ray powder diffraction and can be understood in conjunction with the changes of the nanostructure involved. The real structure of phases $Sb_2Te_3(GeTe)_n$ (n = 3−19) has been investigated by high-resolution electron microscopy (HRTEM) and scanning transmission electron microscopy (STEM)-high-angle annular dark-field (HAADF) with respect to the stoichiometry and synthesis conditions. The correlation of the nanostructure with the thermoelectric properties opens an interesting perspective for tuning thermoelectric properties.

KEYWORDS: GST materials, thermoelectric properties, TEM, real structure elucidation, structure−property relationships

1. INTRODUCTION

Tellurides as Thermoelectrics. Tellurides have been the predominant materials for thermoelectric applications in the past decade. PbTe, Bi_2Te_3, and Sb_2Te_3 are well-established examples that still dominate the market.[1] In order to secure the future energy supply, the sustainable usage of energy is becoming increasingly important.[2] Thermoelectric materials make electric power generation from waste heat possible, e.g., in cars and airplanes, leading to lower fuel consumption. In addition, they may become increasingly popular in energy-efficient cooling and heating devices. The bottleneck for all applications is the efficiency of the transformation between heat and electric energy, which depends on the thermoelectric figure of merit (ZT) of the material used. At a given temperature T, it is defined as:

$$ZT = \frac{S^2\sigma}{\kappa}T$$

The major problem is the interdependence of the material properties determining ZT. The electrical conductivity (σ) and the electronic part of the thermal conductivity (κ_e), which corresponds to heat transport by electrons, are linked by the Wiedemann−Franz law. Both properties correlate with the Seebeck coefficient (S), as all these properties depend on the charge carrier concentration. The phononic part of the thermal conductivity (κ_L) reflects the heat that is transported by phonons. Since it depends on various structural features, it seems to be the most promising approach to reduce κ_L by increased phonon scattering. Therefore, many new approaches rely on nanostructuring and doping. Novel element combinations, e.g., Ag/Sb/Pb/Te (LAST, ZT up to 2)[3] or Ag/Ge/Sb/Te (TAGS, ZT up to 1.5[4]), and structuring processes (e.g., spin-milled, ball-milled and hot pressed crystalline ingots of Bi−Sb−Te alloys with ZT up to 1.4[5]) have led to drastic improvements in recent years. However, there is still an urgent need for bulk materials with high ZT values at various temperatures.

$Sb_2Te_3(GeTe)_n$ as Phase-Change Materials. For rewritable optical data storage media, GST (Ge−Sb−Te) materials have been used for more than a decade[6,7] because the fast reversible phase change between metastable crystalline and amorphous phases can be induced in a favorable energy range. Compared to rewritable DVDs, the GeTe content has been increased for rewritable Blu-Ray discs in order to (1) optimize the bit density by enhancing the difference in reflectivity between both phases and (2) obtain higher stability of the amorphous phase (recording marks), corresponding to a longer life cycle.[8] The fast reversible phase change can also be induced by electric

Received: June 16, 2011
Revised: August 21, 2011
Published: September 12, 2011

dx.doi.org/10.1021/cm201717z | Chem. Mater. 2011, 23, 4349–4356

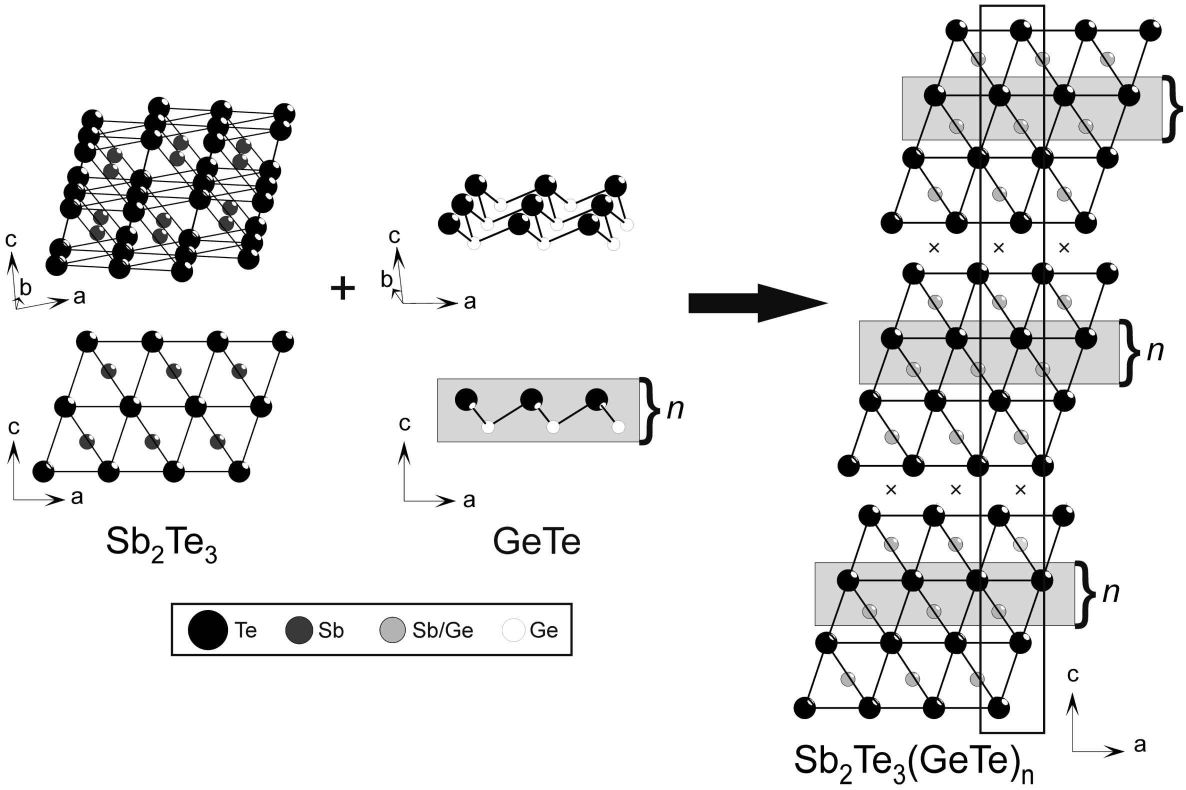

Figure 1. Tetradymite-like Sb_2Te_3 slabs (left) are formally enlarged by inserting GeTe-type layers in the blocks. The resulting structure (right) consists of distorted rocksalt-type building blocks with a thickness depending on the GeTe content *n* (the crosses indicate the position of the formal "vacancies" in the van der Waals gaps). For Sb_2Te_3 itself, *n* equals 0.

pulses, and the structural states can be identified by their different resistivity.[9,10] As the information is preserved by structural changes, GST materials are very promising candidates for nonvolatile PC-RAM devices.[11−14] Besides this well-known phase change between amorphous and metastable crystalline phases, GeTe-rich GST materials exhibit another phase transformation between a rocksalt-type high-temperature and a layered low-temperature modification.

Structure and Properties of $Sb_2Te_3(GeTe)_n$. The structures of materials with the composition $Sb_2Te_3(GeTe)_n$ can be described as a combination of tetradymite-type Sb_2Te_3[15] and GeTe, a binary variant of the A7 (gray arsenic) structure type. The tetradymite-like Sb_2Te_3 blocks can formally be enlarged by inserting GeTe, resulting in the pseudobinary homologous series $Sb_2Te_3(GeTe)_n$ with distorted rocksalt-type building blocks of a thickness depending on *n* (Figure 1). These blocks are separated by van der Waals gaps between the Te layers terminating the individual building blocks. The distance between these Te layers and the following cation layers are rather short, leading to a 3 + 3 coordination of these cations and an arrangement resembling that in GeTe itself. The Te−Te distances between adjacent building blocks are significantly shorter than the sum of the van der Waals radii and indicate partially covalent bonding. Although these trigonal, thermodynamically stable phases contain no structural vacancies, the strongly distorted octahedral voids between these Te layers can formally be viewed as layer-like ordered cation-position "vacancies".[16,17] The cubic rocksalt-type high-temperature phases are highly disordered with Ge, Sb, and vacancies occupying the cation positions and Te occupying the anion positions. The vacancy concentration depends on the ratio $GeTe/Sb_2Te_3$ (*n*).[18,19] In GeTe rich ($n > 3$) GST phase-change materials, the structure of the crucial metastable crystalline phase is similar to the high-temperature rocksalt-type phase. It is kinetically inert at ambient conditions, providing long-time data storage on rewriteable optical media.

In recent years, the thermoelectric behavior of some GST materials has been investigated.[20] HRTEM investigations of spark plasma sintered $Sb_2Ge_{0.02}Te_3$ revealed a large number of randomly distributed nanodomains, coupled with a 0.3 W/mK decrease in thermal conductivity compared to pure Sb_2Te_3. Consequently, the *ZT* value of Sb_2Te_3 increases from 0.74 to 0.84 at 492 K when doped with small amounts of Ge.[21] Recent investigations indicate *ZT* values up to 1.3 at 720 K for Ge-rich compositions ($n \sim 12$).[22]

2. EXPERIMENTAL SECTION

Bulk samples of $Sb_2Te_3(GeTe)_n$ ($3 \leq n \leq 19$) were prepared by melting (950 °C, 2 h) stoichiometric amounts of the elements Ge (99.999%, Sigma Aldrich), Sb (99.999%, Smart Elements), and Te (99.999%, Alfa Aesar) in silica glass ampules sealed under Ar atmosphere. Nanostructured samples were obtained by annealing the initially quenched samples at 500−550 °C (i.e., in the stability range of the cubic high-temperature phase) for 2 days and quenching in water. The relaxed (trigonal) samples with less pronounced nanostructuring were annealed for 2 days at 400 °C and slowly cooled in the furnace (2 h). A fraction of each sample was used for electron microscopy.

Ingots for thermoelectric measurements were prepared under analogous conditions in silica glass ampules with flat bottom. The ingots obtained were disk-shaped with a diameter around 15 mm and a thickness of 2−6 mm. They were polished to obtain flat discs with a

Table 1. Phase Transformation Temperatures of $Sb_2Te_3(GeTe)_n$ ($3 \le n \le 17$) from Temperature Programmed XRPD

composition	T1 (in °C)	T2 (in °C)	T3 (in °C)
$Sb_2Te_3(GeTe)_3$	375	560	550
$Sb_2Te_3(GeTe)_7$	250−320	500	460
$Sb_2Te_3(GeTe)_{12}$	325	475−500	460
$Sb_2Te_3(GeTe)_{14}$	325	450	320
$Sb_2Te_3(GeTe)_{17}$	300	410	250−275

constant thickness. X-ray powder diffraction patterns matched those from corresponding samples used for other investigations.

The composition of the samples was verified by energy-dispersive X-ray spectroscopy (EDX). Typical analyses deviate less than 5 atom % from values corresponding to the starting mixture. Data acquisition was done using a JSM-6500F (Jeol, Japan) scanning electron microscope equipped with an EDX detector (model 7418, Oxford Instruments, UK).

For transmission electron microscopy, samples were finely ground, dispersed in ethanol, and subsequently transferred on a copper grid coated with holey carbon film. Selected area electron diffraction (SAED) and high-resolution electron microscopy (HRTEM) were done on a JEM2011 (Jeol Ltd., Japan) with an tungsten thermal emitter and an acceleration voltage of 200 kV equipped with a TVIPS CCD camera (model 114, resolution: 1k × 1k). Further HRTEM, SAED, EDX, and scanning transmission electron microscopy (STEM) using a high-angle annular dark-field (HAADF) detector was done on a Titan 80-300 (FEI, USA) with a field emission gun operated at 300 kV equipped with a TEM TOPS 30 EDX spectrometer (EDAX, Germany). Images were recorded on an UltraScan 1000 camera (Gatan, USA, resolution: 2k × 2k). HRTEM and SAED data were evaluated using the Digital Micrograph[23] and EMS[24] software; for STEM and EDX data, the program ES Vision[25] was used.

X-ray powder diffraction (XRPD) patterns were recorded from ground samples fixed on Mylar foils using silicone grease. Data were collected on a G670 Guinier camera (Huber, Germany) equipped with a fixed imaging plate detector with an integrated read-out system using Cu $K\alpha_1$ radiation (Ge monochromator, λ = 1.54051 Å).

Temperature programmed XRPD patterns were collected using powdered samples filled into silica glass capillaries with a diameter of 0.3 mm and sealed with silicone grease under Ar. Data were collected using a Stadi P powder diffractometer (Stoe & Cie. GmbH, Germany) with a linear position-sensitive detector (PSD) and a graphite furnace using Mo $K\alpha_1$ radiation (Ge monochromator, λ = 0.71093 Å). The samples were heated from room temperature to 600 °C (10°/min) and subsequently cooled to room temperature in the same way. Data were collected every 25 °C with 10 min acquisition time. Powder patterns were analyzed with WIN^{XPOW}.[26]

Thermoelectric properties were measured up to 450 °C under vacuum using commercial and in-house-built facilities of the DLR (Cologne, Germany). The Seebeck coefficient was measured by establishing a small temperature gradient across the sample while the temperature was changed slowly and continuously. Type-R thermocouples attached directly to the sample's surface were used for both temperature measurement (T_1 and T_2) and Seebeck voltage (U_S) pickup via the Pt lines. The sample's Seebeck coefficient was then calculated as

$$S_{\text{sample}} = \frac{U_S}{\Delta T} - S_{\text{Pt}} \qquad \Delta T = |T_2 - T_1|$$

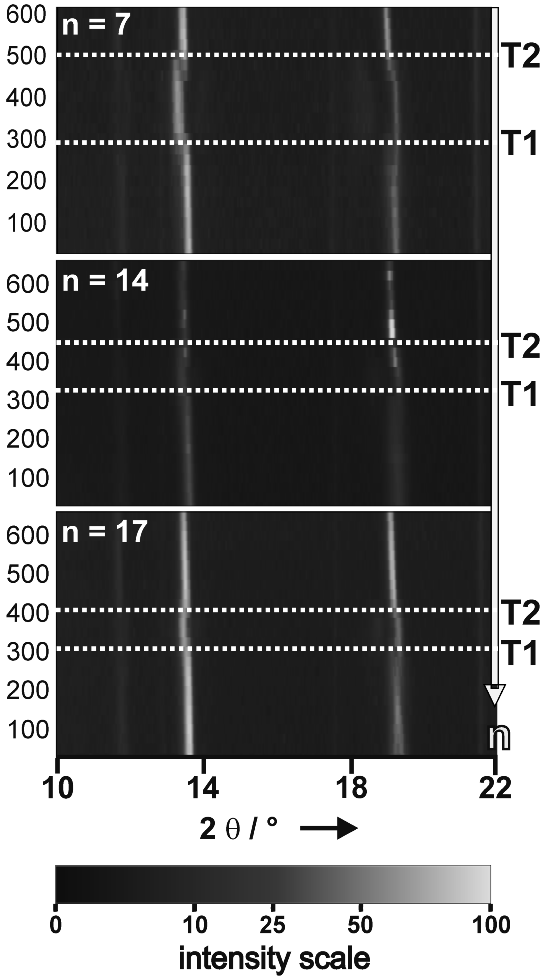

Figure 2. Heating section of the temperature-dependent PXRD of different $Sb_2Te_3(GeTe)_n$ samples with the transition temperatures T1 and T2 (left: temperatures in °C).

Electrical conductivity σ was calculated from the sample's resistance R, measured using an AC method in order to reduce Peltier influences and a four-point-probe setup to avoid cable and contact resistances affecting the measurement. When the cross-section A of the sample and the distance l of the probe tips are taken into account, the electrical conductivity follows as $\sigma = l/A\,R$. Thermal conductivity κ was calculated from measurements of the thermal diffusivity D_{th} using a laser-flash apparatus (LFA 427, Netzsch GmbH & Co., Germany), the heat capacity c_p in a differential scanning calorimeter (DSC 404, Netzsch GmbH & Co., Germany), and the density ρ using a Mohr's balance: $\kappa = D_{\text{th}} \cdot \rho \cdot c_p$.

3. RESULTS AND DISCUSSION

Stability of the Phases $Sb_2Te_3(GeTe)_n$ ($3 \le n \le 17$). Temperature-dependent XRPD investigations of quenched samples of $Sb_2Te_3(GeTe)_n$ ($3 \le n \le 17$) were performed in order to determine the existence range of the different phases (Table 1). Two changes occur when the quenched samples are heated (T1, T2) (Figure 2) and one during cooling (T3) (Table 1). All transformation temperatures depend on the composition, indicating the influence of the thickness of the distorted rocksalt-type building blocks and the vacancy concentration on the stability of each phase, respectively. Starting from quenched pseudocubic samples, diffusion processes occur at T1 when the quenched sample with short-range ordered vacancies relaxes to the thermodynamically stable trigonal phase (see below), which transforms to the cubic high-temperature phase when the sample reaches the latter's

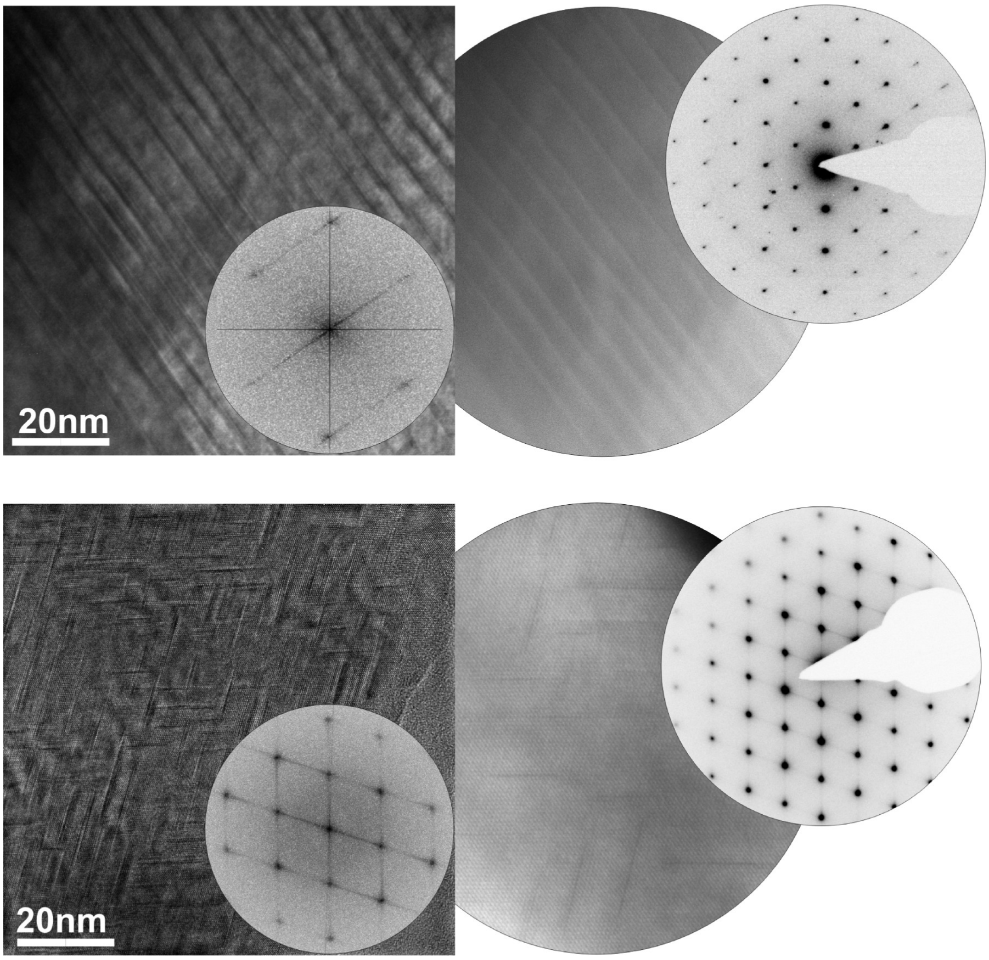

Figure 3. Comparison of two samples of $Sb_2Te_3(GeTe)_{12}$ with different thermal treatment (top: annealed at 400 °C for 20 h; bottom: quenched from 500 °C); each with HRTEM image (left, inset: corresponding Fourier transform), STEM-HAADF image (middle), and SAED (right).

stability region (T2). When it is slowly cooled below that stability range, the transformation from the cubic to the trigonal phase occurs (T3). This phase transition is delayed because the high-temperature phase can be undercooled (T3 < T2).

With increasing GeTe content *n*, the cubic phase obviously becomes more stable and more inert at lower temperatures: it is reached at lower temperatures (T2) upon heating and can be increasingly undercooled (T3 decreases). GeTe itself cannot be undercooled as it exhibits no vacancies.[27] Its transition temperature (ca. 390 °C for slightly Te-rich samples) between the rhombohedral and the cubic phase continues the trend given by samples with increasing *n*.

The diffusion pathways required to reach the trigonal phase with more or less equidistant van der Waals gaps depend on the block size. Due to the long diffusion pathways involved, the cubic phase can be increasingly undercooled and partially retained at room temperature by quenching the samples if the GeTe content is higher (i.e., thicker blocks). The transition from the trigonal to the cubic phase requires a rearrangement of the Te substructure and the introduction of randomly distributed structural vacancies on cation positions. This process is governed by thermodynamics rather than by kinetics. Trigonal phases of all samples investigated can be long-time annealed at 400 °C without phase transition to the cubic high-temperature phase.

Influence of Thermal Treatment on the Nanostructure. The microstructure of $Sb_2Te_3(GeTe)_{12}$ samples with different thermal treatment have been investigated by TEM. Samples quenched from temperatures in the existence range of the cubic high-temperature phase show intersecting defect layers perpendicular to all pseudocubic ⟨111⟩ directions in the HRTEM images. A parquet-like structure is formed, and corresponding diffuse intensities are observed in the SAED patterns (Figure 3). The defect layers are directly imaged by Z contrast in STEM-HAADF images (electron-rich areas appear brighter). A similar HRTEM investigation of samples that were annealed in the existence range of the trigonal phase (400 °C) show parallel van der Waals gaps with irregular distances, which can only formally be viewed as “defect layers”. Accordingly, the corresponding SAED patterns show diffuse intensities only in the direction orthogonal to the layers (Figure 3). Slowly cooled samples resemble those obtained by annealing quenched ones.

The different arrangements of the defect layers or van der Waals gaps, respectively, are a consequence of the diffusion processes that occur during the phase changes associated with the thermal treatment. The disorder−order phase transition from the cubic high-temperature phase with random distribution of the vacancies to the long-range ordered trigonal structures, which are thermodynamically stable at room temperature, requires a reconstructive phase transition including a rearrangement of the

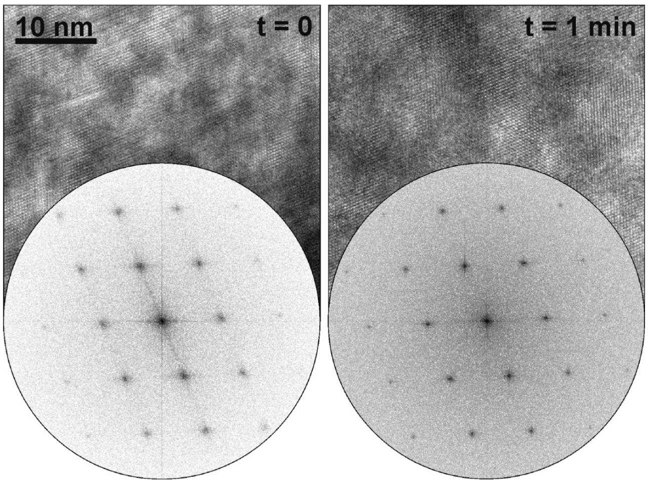

Figure 4. Quenched sample with diffuse intensities in the corresponding Fourier transform and defect layers in HRTEM (left); after prolonged exposition (1 min) to the electron beam, there are no diffuse intensities in the Fourier transform and no defect layers in HRTEM (right).

anion substructure. During this phase transformation, the short-range order gradually increases when the vacancies are arranged in two-dimensional layers by diffusion in the solid state. In quenched phases, the defect layers are finite and arranged perpendicular to all ⟨111⟩ directions of the original cubic phase, forming the parquet-like structure consisting of multiple intersecting defect layers. Annealing quenched phases leads to further diffusion and thus to an extension of the defect layers toward the thermodynamically stable trigonal phase with an ideally symmetric, equidistant arrangement of van der Waals gaps. Summing up, the structure of the quenched phases combines features of both stable (low and high temperature) phases even though it cannot be observed as an intermediate state during the phase transition at equilibrium conditions.

Investigations of the phase diagram Ge−Sb−Te showed that such samples need up to 8 months of annealing to reach the trigonal thermodynamically stable phase.[28] Therefore, it is possible to obtain various stages between the structure of quenched samples and the stable phase by controlling the annealing conditions. This transformation is hindered because the cubic structure is locally preserved, owing to stresses caused by multiple twinning that is unavoidable in quick transitions from the cubic high-temperature to the rhombohedral phase (*translationengleiche* group-subgroup relationship).[30] When the quenched pseudocubic samples are heated, the mobility of vacancies increases and stresses are relieved during the transformation to the stable trigonal structure (T1 in Table 1).

In situ TEM experiments show that the defect layers present in samples quenched from the cubic high-temperature phase disappear when the sample is exposed to the highly energetic electron beam for about 1 min (Figure 4). This is similar to the behavior described for $Ge_2Sb_2Te_5$.[29]

Influence of the Composition on the Nanostructure of Quenched $Sb_2Te_3(GeTe)_n$ Samples. The nanostructure of $Sb_2Te_3(GeTe)_n$ ($n = 4.5-19$) samples quenched from the cubic phase not only depends on the thermal treatment but also on the composition (n) of the samples. Higher GeTe contents result in fewer defects in the high-temperature phase and larger blocks in the trigonal phase with strongly varying thicknesses. Higher

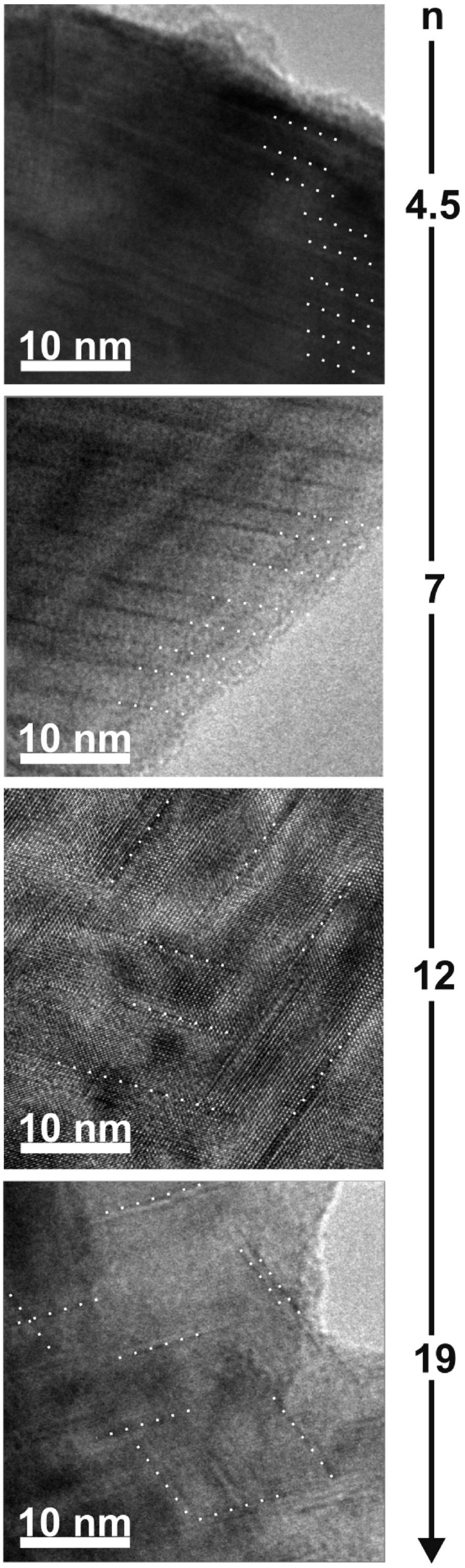

Figure 5. HRTEM images of different $Sb_2Te_3(GeTe)_n$ samples with similar thermal treatment (top to bottom n = 4.5; 7; 12; 19; the defect layers are highlighted with white dotted lines); they become fewer and less regularly spaced with increasing n.

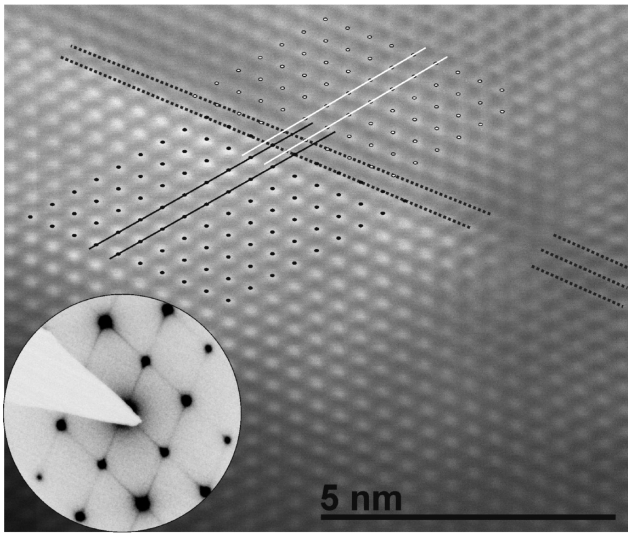

Figure 6. STEM-HAADF image (pseudocubic zone axis ⟨110⟩, with corresponding SAED of the whole crystallite) of $Sb_2Te_3(GeTe)_{12}$; the atom rows on either side of the defect layer are marked (gray and white dotted lines); at the defect layer, the structure is shifted by 1/3 of the distance between the atom rows parallel to the defect layer; the image also shows the relaxation of the defect layer (black lines).

defect concentrations at lower GeTe contents correspond to an increased number of van der Waals gaps with more regular spacing (Figure 5). This change in the variance of the spacing results from the increasing diffusion pathways which are necessary to reach the ideal, thermodynamically stable trigonal phase. Samples with a higher GeTe content must be annealed much longer in order to reach this state, and therefore, the block thickness distribution is more irregular as compared to samples with the same thermal treatment and a lower GeTe content.

Increased diffusion pathways have a second effect on the microstructure. The probability of intersecting defect layers with different orientations increases when the diffusion pathways necessary to form the stable phase increase. Therefore, the fraction of domains with intersecting defect layers forming parquet-like structures increases with the GeTe content. Thus, in addition to the thermal treatment, the composition is an important factor that determines the nanostructure of $Sb_2Te_3(GeTe)_n$.

Structural Relaxation around the Defect Layers in Sb_2Te_3-$(GeTe)_{12}$. We reported in earlier works that the relaxation and/or shift of Te atom layers upon "vacancy ordering" leads to van der Waals gaps rather than defect layers in an undistorted matrix.[22,30] High-resolution imaging both by HRTEM and STEM-HAADF shows that the magnitude of relaxation between the distorted rocksalt-like building blocks depends on the lateral extension of the "vacancy" layers. Where they terminate, the relaxation is hindered by the surrounding bulk and the Te atom positions of the rocksalt-type phase are approximately retained. For the same reason, no relaxation occurs if the defect layers extend over just a few unit cells. Whenever defect layers extend over larger areas, Te−Te contacts are formed and the structure is partially relaxed (Figure 6). The relaxation includes a shift of 1/3 of the distance between the rows of atom columns parallel to the defect layers. This shift corresponds to the structure around the van der Waals gaps in stable trigonal phase (compare Figure 1), whose structures were derived from single-crystal data.[31,32] This proves the van der Waals character of extended defect layers whereas less extended ones are rather similar to "point defects" (point defect = a type of defect as opposed to a planar defect or a line defect) with little influence on the surrounding lattice.

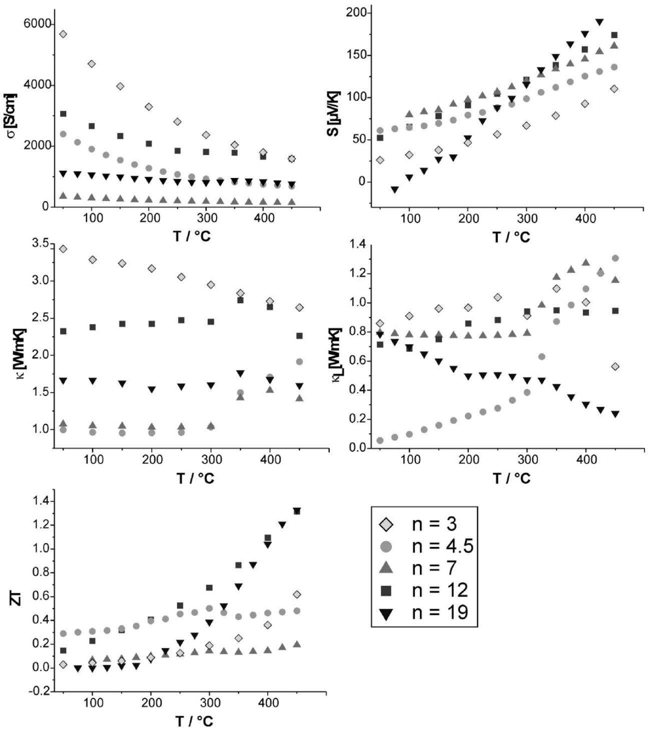

Figure 7. Thermoelectric characteristics of quenched $Sb_2Te_3(GeTe)_n$ (n = 3−19) samples; electric conductivity (σ) (top left); Seebeck coefficient (S) (top right); thermal conductivity (κ) (middle left); lattice thermal conductivity (κ_L) (middle right), and the resulting thermoelectric figure of merit (ZT, bottom).

Influence of the Microstructure on the Thermoelectric Characteristics of $Sb_2Te_3(GeTe)_n$ (n = 3−19). The thermoelectric properties of $Sb_2Te_3(GeTe)_n$ (n = 3, 4.5, 7, 12, 19) samples, each quenched from its cubic high-temperature phase, show that the nanostructures resulting from different compositions (Figure 7) have diverse and, in part, complex consequences.

For all samples of $Sb_2Te_3(GeTe)_n$ with n = 3−19, the Seebeck coefficients (S) are quite similar and increase continuously with the temperature reaching 100−200 $\mu V\,K^{-1}$ at 450 °C. They correspond to p-type semiconductors. For n = 19, the increase with the temperature is most pronounced. Such values are common for materials with high ZT values, e.g., TAGS (Te−Ag−Ge−Sb) compounds with S = 160−220 μV/K at 450 °C, the exact values depending on the composition and sample treatment.[33,34] Water quenched and rapidly solidified (melt-spun) samples of layered $Sb_2Te_3(GeTe)_n$ with n = 1 or 2 reach S = 60−110 μV/K at 450 °C.[35]

The temperature dependence of the electrical conductivity (σ) corresponds to metallic behavior. Upon heating, σ decreases down to 800−2000 S/cm at 450 °C, which is also similar to TAGS compounds (800−1200 S/cm at 450 °C)[33,34] and optimized $Sb_2Te_3(GeTe)_n$ (n = 1, 2) (1500−2000 S/cm at 450 °C).[35] The electrical conductivity decreases with the GeTe content for n = 3, 4.5, 7, probably as a consequence of the increasingly inhomogeneous spacings between defect layers (see above). Further increasing the GeTe content (n = 12, 19) increases σ, probably because the defect layer concentration gets rather small and its influence on the metallic character becomes less dominant. The fact that $Sb_2Te_3(GeTe)_{12}$ exhibits the maximal electrical conductivity is probably the result of a complex interplay of different factors.

As the positive effect of a high electrical conductivity σ is compensated by a higher electronic part of the thermal conductivity κ_e, the phononic part (lattice thermal conductivity κ_L) is crucial for *ZT*. The overall thermal conductivities of the compounds $Sb_2Te_3(GeTe)_n$ (n = 3−19) range from 1 to 3.5 W/mK, the lattice part amounts to 0.2−1.3 W/mK at 450 °C. For TAGS, the overall thermal conductivity ranges from 1.5 to 2.8 with a lattice part around 0.4 at 450 °C.[33,34]

In general, more pronounced nanostructuring is expected to cause more phonon scattering and thus reduce κ_L, thereby increasing *ZT*. Higher defect concentrations should have a similar effect. $Sb_2Te_3(GeTe)_3$ has the highest overall thermal conductivity of the samples investigated. Its cubic high-temperature phase exhibits a maximum cation defect concentration; however, it cannot be quenched to a pseudocubic one with highly disordered defect planes. Therefore, quenched samples of $Sb_2Te_3(GeTe)_3$ are not significantly different from annealed ones and exhibit an almost completely ordered trigonal structure with equidistant van der Waals gaps. Since such an ordered arrangement has less potential to suppress the phonon proliferation, $Sb_2Te_3(GeTe)_3$ has the highest lattice (κ_L) and overall (κ) thermal conductivity. This results in a relatively low *ZT* value. Therefore, the rather low *ZT* of more or less long-range ordered phases $Sb_2Te_3(GeTe)_n$ with n = 1 or 2 (∼0.2 at 450 °C)[35] is not surprising.

Since *ZT* of all compounds investigated increases with temperature, the temperature dependence of κ_L is crucial. $Sb_2Te_3(GeTe)_{4.5}$ has a very low κ_L and thus the highest *ZT* at room temperature, probably due to the high defect concentration combined with disorder. However, in this case, the diffusion pathways are rather short so that the transition to the stable trigonal phase causes κ_L to increase significantly with the temperature. That outweighs the increasing Seebeck coefficient and results in a comparably low *ZT* at higher temperatures. The same effect is observed for $Sb_2Te_3(GeTe)_7$ which has a higher κ_L at room temperature due to the reduced defect concentration and therefore a lower *ZT* value. The overall low thermal conductivity is not helpful as it comes with a low electrical conductivity. The lower defect concentration also means less pronounced effects of structural changes at higher temperatures since the diffusion pathways are significantly increased compared to $Sb_2Te_3(GeTe)_{4.5}$. The compounds with higher GeTe contents (n = 12, 19) increasingly show the parquet-like structure, owing to intersecting finite defect layers as a result of the even longer diffusion pathways hypothetically required to form the thermodynamically stable trigonal phase. The diffusion processes are, of course, more pronounced at higher temperatures, which results in an increased κ_L, except for $Sb_2Te_3(GeTe)_{19}$, where there is little diffusion due to the low defect concentration. The strongly increasing Seebeck coefficient of the compounds with n = 12 and 19 leads to the steep increase of *ZT* at higher temperatures. As a result, the *ZT* values reach 1.3 at 450 °C for both $Sb_2Te_3(GeTe)_{19}$ and $Sb_2Te_3(GeTe)_{12}$.

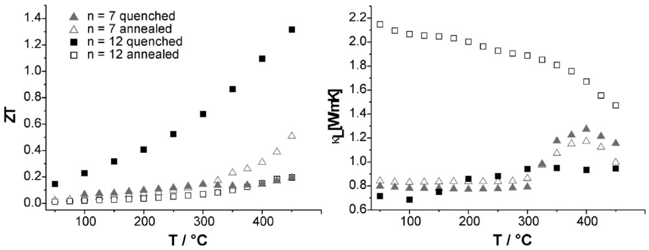

Figure 8. Comparison of the thermoelectric characteristics of quenched samples of $Sb_2Te_3(GeTe)_n$ (n = 7, 12) with those of annealed and slowly cooled ones; left side: thermoelectric figure of merit (*ZT*); right side: lattice thermal conductivity. (κ_L).

In order to analyze the influence of the nanostructure on the thermoelectric properties independent of the chemical composition and the associated carrier concentration, samples with identical composition but different thermal treatment were investigated. Quenched samples of $Sb_2Te_3(GeTe)_{12}$ and $Sb_2Te_3(GeTe)_7$ have a higher *ZT* value at room temperature than those annealed at 400 °C (in the stability range of the trigonal phase) and slowly cooled afterward (Figure 8). The Seebeck coefficients are influenced very little by the thermal treatment and almost identical for the samples investigated. Up to 300 °C, i.e., in the temperature range where diffusion effects are negligible, the lattice thermal conductivity of the quenched samples is significantly lower, reflecting the high degree of phonon scattering by the finite defect layers with irregular spacings. This effect is much more pronounced in $Sb_2Te_3(GeTe)_{12}$ than it is in $Sb_2Te_3(GeTe)_7$. This is obviously due to the parquet-like structure of quenched $Sb_2Te_3(GeTe)_{12}$ which is neither present in annealed samples nor in quenched $Sb_2Te_3(GeTe)_7$.

The electrical conductivity σ of annealed and slowly cooled $Sb_2Te_3(GeTe)_{12}$ is lower than that of quenched samples. For $Sb_2Te_3(GeTe)_7$, however, σ nearly doubles between 300 and 400 °C, resulting in a higher *ZT* value at high temperatures than that of quenched samples. The slowly cooled samples exhibit a structure that is closer to the thermodynamically stable layered structure than that of the quenched sample. Most defect layers in slowly cooled $Sb_2Te_3(GeTe)_{12}$ are already ordered and form van der Waals gaps, which results in long diffusion pathways for the remaining disordered defects. This results in a decreasing lattice thermal conductivity with increasing temperatures, comparable to the situation in quenched $Sb_2Te_3(GeTe)_{19}$. Thus, the high ZT value of quenched $Sb_2Te_3(GeTe)_{12}$ is a consequence of the reduced thermal conductivity in combination with a high electrical conductivity.

4. CONCLUSION

The nanostructure of $Sb_2Te_3(GeTe)_n$ (n = 3−19) can be tuned both by varying the composition and by changing the thermal treatment of the samples. Cation defects tend to form layers, which become van der Waals gaps if they are extended enough to allow the relaxation of the surrounding structure. Quenching from highly disordered cubic high-temperature phases leads to finite intersecting defect layers forming a parquet-like structure, which (especially for n = 12) leads to a significant reduction of the lattice thermal conductivity. The concentration and arrangement of the defect layers have substantial influence on the thermoelectric properties. The temperature dependence of the individual contributions varies in a rather complicated way. Although this makes predictions rather difficult, the complex interplay of different structural features correlates with the properties and is very valuable for an a posteriori understanding many observed effects.

The Seebeck coefficient of all compounds investigated rises with increasing temperature, especially for high GeTe contents, and indicates p-type semiconductors. Materials with intermediate *n* such as $Sb_2Te_3(GeTe)_7$ have the lowest electric conductivity. As their lattice thermal conductivity increases with temperature, they interestingly exhibit the lowest *ZT* values at high temperatures, in addition to those (e.g., $n = 3$) that exhibit fully ordered structures independent of the thermal treatment. A high defect concentration leads to a relatively homogeneous arrangement of parallel "defect layers" which correspond to van der Waals gaps and result in an increased electric conductivity. The high defect concentrations induces a low lattice thermal conductivity in case enough disorder remains in quenched pseudocubic samples. This holds for GeTe contents as low as $n = 4.5$; further decreasing *n* is not helpful as short diffusion pathways usually yield highly ordered structures (as shown for $n = 3$). The increased mobility of the atoms at higher temperatures emphasizes the importance of order−disorder effects and causes a more or less pronounced transition to the thermodynamically stable phase with equidistant van der Waals gaps around ~300 °C. In compounds with higher GeTe contents, the reduced defect concentration increases the electrical conductivity while the long diffusion pathways required to form extended defect layers result in intersecting finite defect layers and a more pronounced nanostructure, decreasing the lattice thermal conductivity (especially for $n = 19$). Therefore, the compounds $Sb_2Te_3(GeTe)_{12}$ and $Sb_2Te_3(GeTe)_{19}$ have rather low *ZT* values at room temperature but reach the highest *ZT* values up to 1.3 in the high-temperature range. Although due to limited long-time stability above ~300 °C, this value has little meaning for the application in actual devices; the *ZT* values of about 0.7 in the temperature interval where the nanostructures are long-time stable still seems promising. Probably, the properties can be further enhanced by doping with additional elements, even if such efforts might further complicate the situation. In contrast to other multinary telluride systems, germanium antimony tellurides do not tend to exhibit phase separation (e.g., precipitates) and, despite the nanostructuring, remain chemically homogeneous.

AUTHOR INFORMATION

Corresponding Author

*Fax: (+49)89-2180-77440. E-mail: oliver.oeckler@gmx.de.

ACKNOWLEDGMENT

The authors thank Christian Minke (LMU Munich) for SEM operation and EDX analyses, Thomas Miller (LMU Munich) for the temperature-dependent powder diffraction experiments, and Werner Schönau (DLR Cologne) for temperature-dependent thermal analysis. Furthermore, we are indebted to Prof. Dr. W. Schnick (LMU Munich) for his generous support of this work. This investigation was funded by the Deutsche Forschungsgemeinschaft (grants OE530/1-1 and OE530/1-2).

REFERENCES

(1) Snyder, G. J.; Toberer, E. S. *Nat. Mater.* **2008**, *7*, 105–114.

(2) Schüth, F. *Positionspapier Koordinierungskreis Chemische Energieforschung*, 2009.

(3) Hsu, K. F.; Loo, S.; Guo, F.; Chen, W.; Dyck, J. S.; Uher, C.; Hogan, T.; Polychroniadis, E. K.; Kanatzidis, M. G. *Science* **2004**, *303*, 818–821.

(4) Heremans, J. P.; Jovovic, V.; Toberer, E. S.; Saramat, A.; Kurosaki, K.; Charoenphakdee, A.; Yamanaka, S.; Snyder, G. J. *Science* **2008**, *321*, 554–557.

(5) Poudel, B.; Hao, Q.; Ma, Y.; Lan, Y.; Minnich, A.; Yu, B.; Yan, X.; Wang, D.; Muto, A.; Vashaee, D.; Chen, X.; Liu, J.; Dresselhaus, M. S.; Chen, G.; Ren, Z. *Science* **2008**, *320*, 634–638.

(6) Wuttig, M.; Yamada, N. *Nat. Mater.* **2007**, *6*, 824–832.

(7) Raoux, S. *Annu. Rev. Mater. Res.* **2009**, *39*, 9.1–9.24.

(8) van Pieterson, L.; Lankhorst, M. H. R.; van Schijndel, M.; Kuiper, A. E. T .; Roosen, J. H. J. *J. Appl. Phys.* **2005**, *97*, 083520.

(9) Ovshinsky, S. R. *Phys. Rev. Lett.* **1968**, *21*, 1450–1452.

(10) Welnic, W.; Wuttig, M. *Mater. Today* **2008**, *11*, 20–27.

(11) Raoux, S.; Shelby, R. M.; Jordan-Sweet, J.; Munoz, B.; Salinga, M.; Chen, Y.-C.; Shih, Y.-H.; Lai, E.-K.; Lee, M.-H. *Microelectron. Eng.* **2008**, *85*, 2330–2333.

(12) Wuttig, M.; Steimer, C. *Appl. Phys. A: Mater. Sci. Process.* **2007**, *87*, 411–417.

(13) Lacaita, A. L.; Wouters, D. J. *Phys. Status Solidi A* **2008**, *205*, 2281–2297.

(14) Terao, M.; Morikawa, T.; Ohta, T. *Jpn. J. Appl. Phys.* **2009**, *48*, 080001.

(15) Anderson, T. L.; Krause, H. B. *Acta Crystallogr.* **1974**, *C47*, 1141–1143.

(16) Karpinsky, O. G.; Shelimova, L. E.; Kretova, M. A.; Fleurial, J.-P. *J. Alloys Compd.* **1998**, *268*, 112–127.

(17) Shelimova, L. E.; Karpinsky, O. G.; Kretova, M. A.; Kosyakov, V. I.; Shestakov, V. A.; Zemskov, V. S.; Kuznetsov, F. A. *Inorg. Mater.* **2000**, *36*, 768–775.

(18) Matsunaga, T.; Morita, H.; Kojima, R.; Yamada, N.; Kifune, K.; Kubota, Y.; Tabata, Y.; Kim, J.-J.; Kobata, M.; Ikenaga, E.; Kobayashi, K. *J. Appl. Phys.* **2008**, *103*, 093511.

(19) Raoux, S.; Wojciech, W.; Ielmini, D. *Chem. Rev.* **2010**, *110*, 240–267.

(20) Yan, F.; Zhu, T. J.; Zhao, X. B.; Dong, S. R. *Appl. Phys. A: Mater. Sci. Process.* **2007**, *88*, 425–428.

(21) Cui, J. L.; Fu, H.; Liu, X. L.; Chen, D. Y.; Yang, W. *Curr. Appl. Phys.* **2009**, *9*, 1170–1174.

(22) Schneider, M. N.; Rosenthal, T.; Stiewe, C.; Oeckler, O. *Z. Kristallogr.* **2010**, *225*, 463–470.

(23) *DigitalMicrograph 3.6.1*; Gatan Software: Brisbane, Australia, 2007.

(24) Stadelmann, P. A. *Ultramicroscopy* **1987**, *21*, 131–145.

(25) *ESVision, 4.0.164*; Emispec Systems Inc.: Tempe, AZ, 1994−2002.

(26) *WINXPOW*, Version 2.12; Stoe & Cie. GmbH: Darmstadt, Germany, 2005.

(27) Chattopadhyay, T.; Boucherle, J. X.; von Schnering, H. G. *J. Phys. C: Solid State Phys.* **1987**, *20*, 1431–1440.

(28) Bordas, S.; Clavaguera-Mora, M. T.; Legendre, B.; Hancheng, C. *Thermochim. Acta* **1986**, *107*, 239–265.

(29) Kooi, B. J.; Groot, W. M. G.; De Hosson, J. T. M. *J. Appl. Phys.* **2004**, *95*, 924–932.

(30) Schneider, M. N.; Urban, P.; Leineweber, A.; Döblinger, M.; Oeckler, O. *Phys. Rev. B* **2010**, *81*, 184102.

(31) Agaev, K. A.; Talybov, A. G. *Sov. Phys. Cryst.* **1966**, *11*, 400–402.

(32) Schneider, M. N.; Oeckler, O. *Z. Anorg. Allg. Chem.* **2008**, *634*, 2557–2561.

(33) Chen, Y.; Zhu, T. J.; Yang, S. H.; Zhang, S. N.; Miao, W.; Zhao, X. B. *J. Electron. Mater.* **2010**, *39*, 1719–1723.

(34) Yang, S. H.; Zhu, T. J.; Yu, C.; Shen, J. J.; Yin, Z. Z.; Zhao, X. B. *J. Electron. Mater.* **2011**, *40*, 1244–1248.

(35) Yan, F.; Zhu, T. J.; Zhao, X. B.; Dong, S. R. *Appl. Phys. A: Mater. Sci. Process.* **2007**, *88*, 425–428.